



Superconducting mixed state phase diagram of κ -(BEDT-TTF) $_2$ Cu(NCS) $_2$
by Monty Marcus Mola

A dissertation submitted in partial fulfillment of the requirements for the degree of Doctor of
Philosophy in Physics
Montana State University
© Copyright by Monty Marcus Mola (2001)

Abstract:

This dissertation explores the superconducting, mixed state phase diagram of the layered organic superconductor κ -(BEDT-TTF) $_2$ Cu(NCS) $_2$. In particular, the melting of the quasi-two-dimensional (Q2D) vortex lattice is investigated throughout a wide range-of the available field and temperature parameter space. At moderate fields (0.01 - 2 tesla) and temperatures (1.5 - 10 kelvin), a cavity perturbation technique is used to study the Josephson plasma resonance. By investigating this phenomenon over a wide frequency, field, and temperature range, one can determine a line in the phase diagram that corresponds to either a flux lattice melting or depinning transition. For high fields (2 - 20 tesla) and low temperatures (0.025 - 0.300 kelvin) cantilever beam torque magnetometry is used to determine the melting of the Q2D flux lattice. In this regime, it is shown that this transition is due to quantum fluctuations in the positions of the vortices. From the results of these two experiments, one can piece together the mixed state phase diagram. Upon doing so, it is seen that the Q2D flux solid and vortex liquid states dominate the majority of the phase diagram.

SUPERCONDUCTING MIXED STATE PHASE DIAGRAM OF

κ -(BEDT-TTF)₂Cu(NCS)₂

by

Monty Marcus Mola

A dissertation submitted in partial fulfillment
of the requirements for the degree

of

Doctor of Philosophy

in

Physics

MONTANA STATE UNIVERSITY
Bozeman, Montana

April 2001

D378
M7309

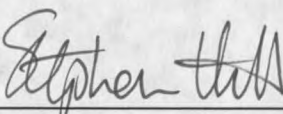
APPROVAL

of a dissertation submitted by

Monty Marcus Mola

This dissertation has been read by each member of the dissertation committee and has been found to be satisfactory regarding content, English usage, format, citations, bibliographic style, and consistency, and is ready for submission to the College of Graduate Studies.

Stephen O. Hill



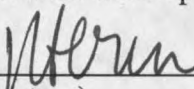
 (Signature)

 4/23/01

 Date

Approved for the Department of Physics

John C. Hermanson



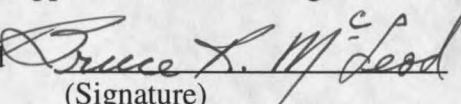
 (Signature)

 4-23-01

 Date

Approved for the College of Graduate Studies

Bruce R. McLeod



 (Signature)

 4-23-01

 Date

STATEMENT OF PERMISSION TO USE

In presenting this dissertation in partial fulfillment of the requirements for a doctoral degree at Montana State University, I agree that the Library shall make it available to borrowers under the rules of the Library. I further agree that copying of this dissertation is allowable only for scholarly purposes, consistent with "fair use" as prescribed in the U.S. Copyright Law. Requests for extensive copying or reproduction of this dissertation should be referred to Bell & Howell Information and Learning, 300 North Zeeb Road, Ann Arbor, Michigan 48106, to whom I have granted "the exclusive right to reproduce and distribute my dissertation in and from microform along with the non-exclusive right to reproduce and distribute my abstract in any format in whole or part."

Signature *Merly M. Mc* Date 4/23/01

ACKNOWLEDGEMENTS

I would like to thank Dr. Stephen Hill for providing me with the opportunity to work on such a rich and exciting project. I would also like to express my deepest appreciation to Norman Williams for his patience and guidance in the machine shop, and Margaret Jarrett for her overwhelming support during the last six years.

Finally, I am truly indebted to my friends and family, who have provided tremendous support during my tenure at MSU. In particular, I would like to thank my wife, Cynthia Kiehn, for her monumental patience while I completed my degree.

TABLE OF CONTENTS

LIST OF TABLES.....	vii
LIST OF FIGURES.....	viii
1. INTRODUCTION.....	1
Low dimensional conductors.....	1
BEDT-TTF based conductors and superconductors.....	1
Measuring the Fermi surface.....	9
Superconductivity.....	14
The phenomenon of superconductivity.....	14
Ginzburg-Landau theory.....	18
Vortex structure.....	26
Relevant energy scales.....	28
2. EXPERIMENTAL TECHNIQUES.....	32
Millimeter-wave measurements.....	32
Introduction.....	32
Technical description.....	33
The MVNA.....	33
The Sample Probe.....	38
The cavities.....	52
Tests.....	61
Torque magnetization measurements.....	68
The cantilever beam torque magnetometer.....	68
Temperature Control.....	71
Conclusion.....	71
3. JOSEPHSON PLASMA RESONANCE IN κ -(ET) ₂ Cu(NCS) ₂	73
Theory.....	73
Classic Josephson effects.....	74
Layered superconductors.....	78
Josephson plasma resonance.....	85
JPR in κ -(ET) ₂ Cu(NCS) ₂	92
Temperature dependence of the JPR.....	97
Frequency dependence of the JPR.....	105
Conclusion.....	109

4. MAGNETIZATION MEASUREMENTS OF κ -(ET) ₂ Cu(NCS) ₂	111
Theory.....	112
General arguments.....	113
The critical state model.....	118
Magneto-thermal instabilities.....	122
Flux jumps in κ -(ET) ₂ Cu(NCS) ₂	127
Analysis of flux jump amplitudes.....	128
Quantum melting of the Q2D vortex lattice.....	134
Conclusion.....	142
5. SUMMARY AND CONCLUSION.....	146
Summary of Results.....	146
General themes for Q2D superconductors.....	149
Future experiments.....	150
REFERENCES CITED.....	152

LIST OF TABLES

Table

1. Penetration depths and coherence lengths for various elemental superconductors.....18
2. Dynamic range achieved for various frequencies in each microwave band.....35
3. Resonance Parameters for different modes obtained in various cavities.....65
4. Superconducting parameters for various materials.....93

LIST OF FIGURES

Figure

1. The nominally flat ET molecule. The carbons (◦) and sulfurs (o) are strongly σ -bonded within the plane of the molecule, while the π -orbitals on the sulfurs lie perpendicular to the plane of the molecule, and are responsible for the conduction properties of ET based CTS.....2
2. The planar benzene ring. The 2s and 2p atomic orbitals for each carbon hybridize, and then overlap with those on adjacent atoms to form strong σ -bonds (left). The left over p orbitals lie normal to the plane of the molecule (right) and form the π -orbitals, with loosely bound electrons.....4
3. Formation of energy bands as a function of inverse inter-atomic spacing. a.) For isolated atoms, the energy levels are discrete, but by b.) bringing many atoms closer together, the energy levels broaden, forming bands.....5
4. The crystal structure of the organic superconductor β -(ET)₂I₃ a.) The unit cell of the material, and b.) looking down the long axis of the ET molecules. The ordering of the ET molecules within the crystal causes the conduction to be preferred along the chains.....6
5. The unit cell of κ -(ET)₂Cu(NCS)₂. a.) The planar organic ET molecules are stacked vertically in the bc-plane with the inorganic anions creating insulating sheets between layers. b.) Looking down the a-axis of the crystal, one can see the stacking of the dimmer pairs within each conducting layer. Due to this stacking arrangement, the conductivity is nearly isotropic within each plane.....7
6. a.) The 2D free electron Fermi circle for κ -(ET)₂Cu(NCS)₂ with no interaction with the Bragg planes. b.) The same Fermi surface once the perturbation has been turned on. The interaction with the Bragg planes creates both a Q1D sheet and a Q2D cylinder.....8
7. The calculated a.) bandstructure and b.) Fermi surface for κ -(ET)₂Cu(NCS)₂ from [2]. The perturbation at the Brillouin zone creates both an open and closed portion of the Fermi surface.....9
8. The free electron Fermi sphere (dashed line) in a magnetic field. The field acts to quantize the available energy states into discrete "Landau tubes". As each tube passes through the Fermi surface, it depopulates, resulting in an oscillatory free energy.....12

9. Low temperature resistance for Hg, from [13]. As the temperature decreases, the resistance follows that of a normal metal, but at the superconducting critical temperature, T_c , there is a sharp drop to zero.....14
10. A superconductor in the Meissner state. Below the critical field, H_c , all magnetic flux is expelled from the interior of the crystal. For type-I superconductors, above H_c , flux penetrates the entire sample as it is driven into the normal state. For type-II superconductors, two critical fields exist. Below H_{c1} all flux is expelled as above, but above this field flux enters the crystal in quantized flux tubes. Above H_{c2} the entire sample is driven normal.....15
11. The penetration depth, λ_L , is the characteristic length for which magnetic fields decay within the interior of a superconductor. It is a direct analog of the skin depth in a metal.....17
12. The variation of $B(r)$ and $\psi(r)$ at the interface between normal and superconducting material for type-I (left) and type-II (right) superconductors. For $\kappa \gg 1$, it is energetically favorable to create as many domain walls as possible. While for $\kappa \ll 1$, the system's energy is minimized by a single interface at the sample surface.....23
13. The mixed state of a type-II superconductor in a uniform magnetic field. S indicates superconducting material, D_n is on the order of λ_L , and $D_s \sim (B_{app}/\Phi_0)^{1/2}$ 24
14. The mean field phase diagram for a general type-II superconductor. As will be seen in later chapters, the actual phase diagram for layered materials is much more complicated.....26
15. The structure of an isolated vortex, for $\kappa \gg 1$. The maximum value of $B(r)$ is approximately $2\mu_0 H_{c1}$28
16. Strings of pancake vortices in a layered superconductor. Due to the strong inter-vortex interaction within the planes, and the weak attraction between vortices in adjacent layers, the 2D sheets decouple at a characteristic field B_{DC}30
17. Schematic diagram of the MVNA, which acts as source and detector for the millimeter-wave measurements.....34
18. The mm-wave experimental apparatus for laboratory fields. The dewar used at the NHMFL is slightly modified to fit into the bore of the resistive magnets.....37

19. A comparison between the insertion losses for stainless steel and silver V band waveguides at room temperature.....41
20. An equivalent LRC circuit of the microwave components of the sample probe. The coupling between various components is modeled as a mutual inductance.....44
21. Simulation of the complex parameters of a wave transmitted through a cavity, with a resonance at 60 GHz, and $Q = 5000$. a. Linear amplitude and phase versus frequency in the complex plane. b. Linear amplitude and phase versus frequency, and c. A_1 and A_2 linear amplitudes versus frequency.....46
22. The effect of a leak wave on the ideal resonance in figure 21. a. The resonance frequency, f_0 , no longer lies on the real axis, thus, f_0 no longer corresponds to the maximum amplitude, resulting in a distortion of the Lorentzian line shapes in b. and c.....48
23. Comparison between the empty cavity response of the sample probe using Au plated and unplated SS sections of waveguide for the lower end of the probe. Custom Microwave Inc. (CMI) [34] professionally plated the sections, currently used in the probe.....52
24. Schematic diagram of the axial cavity construction.....53
25. Schematic diagram of the transverse cavity construction.....56
26. a. The endplate configuration: the sample experiences a transverse H_{AC} .
b. The pillar configuration: the sample experiences an axial H_{AC}58
27. For Q2D samples with the low conductivity axis aligned with the axis of the cavity, a. an axial H_{AC} will drive currents within the highly conducting planes, b. while a transverse H_{AC} will drive current both in the planes as well as along the least conductive direction.....59
28. A real TE₀₁₁ resonance for a loaded axial cavity. The upper panel shows the resonance circle in the complex plane. The squares are raw data and the line is a fit. The lower panel shows the linear amplitude and phase variation as a function of frequency.....62
29. The cavity construction lifts the degeneracy of the TE_{01n} and TM_{11n} modes. The main portion of the figure shows the two resonances separated by 230 MHz. The inset shows the corresponding circles in the complex plane.....63

30. Various cavity resonances plotted as circles in the complex plane, obtained in: a. V – band, b. W – band, and c. D – band. The points are raw data, while the solid lines are fits.....64
31. Comparison between field sweeps with the temperature unlocked (upper) and actively controlled (lower). Broad dip due to impurities in waveguide, prior to Au plating.....66
32. Schematic diagram of the CBTM. The torque experienced by the magnetic moment of the sample causes the capacitance of the device to change as a function of field. This change in capacitance can be measured, and related back to the magnetization of the sample.....70
33. Current-voltage characteristic for an SIS tunnel junction. J_0 is the maximum dissipationless or critical current density across the junction, and 2Δ is the magnitude of the superconducting gap.....74
34. Classic Josephson tunnel junction. Both sides of the capacitor are held at the same electrostatic potential, so only a supercurrent flows across the junction, which depends on the phase difference of the order parameter between the plates.....76
35. Josephson tunnel junction with a potential difference held across the parallel plates. This configuration leads to an alternating current density across the plates, with a natural plasma frequency, $\omega_p^2 = \pi d J_0 / (\epsilon_0 \Phi_0)$78
36. Schematic structure of a layered superconductor: superconducting sheets are separated by thin gaps. For κ -(ET)₂Cu(NCS)₂, the **a**-axis of the crystal runs perpendicular to the conducting planes.....79
37. In a perfect crystal, pancakes line up to form 3D flux tubes in a trigonal lattice.....80
38. Lines of constant phase around an isolated vortex. The normal core of the vortex results in a singularity.....81
39. The mixed state for a clean type-II superconductor in an applied magnetic field of: $B \sim \mu_0 H_{c1}$, $\mu_0 H_{c1} < B < \mu_0 H_{c2}$, and $B \sim \mu_0 H_{c2}$82
40. Q2D flux lattices. Above B_{cr} , the vortices create 2D arrays in each layer, which are nearly independent of the position of the vortices in the adjacent layer.....84

41. Finite temperatures create thermal fluctuations in the position of the vortices. These “flux phonons” may result in a vortex hopping out of the potential well created by a defect, as well as actually melting the flux lattice, if the mean displacements $u_n(\mathbf{r})$ become large.....85
42. Radiation incident on a layered superconductor. The radiation is polarized such that the AC E-field is along the z-axis, the AC H-field is along the y-axis, and the radiation propagates along the x-axis.....86
43. Dissipation versus applied field at 44 GHz for in-plane currents only. Starting from the bottom, the traces corresponds to 1.6 K, 2.3 K, 3.0 K, and 4.0 K, respectively and have been offset for clarity.....94
44. Dissipation versus magnetic field at 76 GHz, for currents driven both parallel and perpendicular to the superconducting planes. The temperature varies from 2 K to 10 K in integer steps. Clearly, a resonant structure is present for this polarization of the microwave radiation.....95
45. Dissipation versus magnetic field for various frequencies, at 2 K. As the measurement frequency increases, the resonance is observed at lower magnetic field.....96
46. Dissipation versus magnetic field at a frequency of 44 GHz, and for temperatures between 2 – 10 K. The main resonance peak is a monotonically decreasing function of temperature (indicated with an arrow), but the low field tails exhibit a “cusp” behavior (illustrated with the dotted line).....98
47. Dissipation versus magnetic field at 111 GHz, and temperatures of 2 –10 K. The anti-cyclotron nature of the JPR moves the resonance field down into the anomalous cusp regime.....99
48. The resonance field versus temperature for various frequencies. The dashed line is a guide for the eye, which separates the anomalous low field and temperature regime from the rest of the field/ temperature phase space.....100
49. The total asymmetric potential well for a Q2D pancake vortex in layer n (solid line). The attraction to the vortex in the adjacent layer, n-1, creates a symmetric potential, which is offset from the symmetric potential created by the combined effects of collective pinning and strong inter-vortex repulsion.....101

50. The phase diagram of the mixed state for κ -(ET)₂Cu(NCS)₂. Open squares correspond to muon spin rotation experiments [49], filled squares refer to local magnetization measurements [62], filled circles are from these JPR measurements [24], open triangles determine the irreversibility line [59, 60], and open diamonds are from measurements of H_{c2} [59].....104
51. Square of the JPR resonance frequency as a function of magnetic field within the vortex liquid phase ($T = 7$ K). The solid line is a powerlaw fit, which indicates that $\omega_p^2 \sim 1/B$, as expected in the liquid state [63].....106
52. Square of the plasma frequency versus magnetic field within the Q2D vortex solid phase ($T = 2.0$ K). The solid line is a powerlaw fit, which indicates a weak to moderate degree of pinning within the crystal.....107
53. Square of the plasma frequency versus $B^{3/2}$, within the vortex solid phase ($T = 2.0$ K). The solid line is an exponential decaying fit, indicative of extremely weak pinning.....109
54. A transport current due to an applied voltage creates a Lorentz force on an isolated vortex, which causes it to move viscously through the superconductor with a velocity v_v115
55. A single vortex (or flux lattice), with enough thermal energy ($V_{pin} \sim k_B T$) will depin.....116
56. Voltage versus current for two superconductors with different critical currents. I_c is defined as the onset of resistive current flow within the superconducting state, due to the viscous vortex motion.....117
57. In the vortex liquid state, unpinned vortices (\circ) can slip past other pinned vortices (\otimes). Such behavior does not occur in the solid phase, since strong inter-vortex interactions maintain large correlated flux bundles.....118
58. A flux gradient forms in the x direction due to a pinned vortex in the flux solid phase. This induces a transport current at the crystal edge, along the y -axis.....119
59. If the magnitude of the flux gradient exceeds the limit set by the critical current density, flux bundles can roll down the flux gradient, as the local pinning potential ~ 0120

60. Bean's model for the critical state. The flux gradient is constant as the vortices creep into (out of) the interior of the sample with an increasing (decreasing) applied field. B^* is the field at which the flux exactly enters the entire crystal on the initial up-sweep, or the field at which the total current density is zero on subsequent up or down sweeps.....121
61. Flux creep rate versus temperature from [13]. Around 0.5 K, the flux creep rate becomes temperature independent, indicative of quantum tunneling becoming the dominant creep mechanism.....126
62. Temperature versus magnetic field for a single crystal of $\text{YBa}_2\text{Cu}_3\text{O}_{7-\delta}$ from [75]. Thermal spikes indicate runaway magneto-thermal instabilities.....127
63. Raw data of the torque on the sample as a function of applied magnetic field, at 25 mK for angles between 79° (outermost) and 16° (innermost). Field sweep direction is indicated with arrows.....128
64. Magnetization versus magnetic field, at 25 mK, for various angles. Arrows show the direction of field sweep. Saw-toothed flux jumps are obvious.....129
65. dM/dH_{app} versus $1/H_{\text{app}}$. After the initial jump, the slope is linear in applied field, indicating $M \propto \ln(H_{\text{app}})$130
66. a. Linearly decreasing angle dependence of the slope of dM/dH vs. $1/H$. b. The linearly decreasing dependence of ΔM , at the flux jump, on $\cos(\theta)$, indicative of the 2D nature of the vortex sheets.....131
67. Magnetization versus magnetic field at a measurement angle of 47° , and at temperatures as indicated in the figure. B^* corresponds to the field at which the net magnetization is zero – see earlier discussion.....132
68. ΔM versus temperature. The solid line is a powerlaw fit, which indicates that the amplitude of the flux jumps scales with temperature as $\Delta M \propto T^{3/2}$133
69. Magnetization versus magnetic field near B_{irr} , for a. small, b. intermediate, and c. large measurement angles.....135
70. The irreversibility field (\wedge) and melting field for two different samples: sample one (\square), and sample two (\circ). The melting field for either sample falls along the 2D GL fit (solid line).....136
71. de-Haas van Alphen oscillations in $\kappa\text{-(ET)}_2\text{Cu(NCS)}_2$. From these quantum oscillations, one is able to determine the measurement angle for a given sample.....137

72. The irreversibility and melting fields as functions of temperature. The irreversibility line shows a linear temperature dependence, while the melting line exhibits definite negative curvature, consistent with a crossover from quantum and thermal fluctuation induced melting ($T < 0.01T_c$) to dislocation (BKT) induced melting ($T > 0.01T_c$).....139
73. Predicted B-T phase diagram for 2D superconducting systems. Notice at $T \sim T_c/100$, there is a crossover in the melting mechanism, resulting in a melting field below $\mu_0 H_{c2}$, from [69].....140
74. The almost complete temperature/field phase diagram for the organic superconductor, κ -(ET)₂Cu(NCS)₂. Nearly the entire mixed state is in either a Q2D vortex lattice or the vortex liquid state.....144
75. The mixed state phase diagram of κ -(ET)₂Cu(NCS)₂. See chapter four for details.....150

ABSTRACT

This dissertation explores the superconducting, mixed state phase diagram of the layered organic superconductor κ -(BEDT-TTF)₂Cu(NCS)₂. In particular, the melting of the quasi-two-dimensional (Q2D) vortex lattice is investigated throughout a wide range of the available field and temperature parameter space. At moderate fields (0.01 – 2 tesla) and temperatures (1.5 – 10 kelvin), a cavity perturbation technique is used to study the Josephson plasma resonance. By investigating this phenomenon over a wide frequency, field, and temperature range, one can determine a line in the phase diagram that corresponds to either a flux lattice melting or depinning transition. For high fields (2 – 20 tesla) and low temperatures (0.025 – 0.300 kelvin) cantilever beam torque magnetometry is used to determine the melting of the Q2D flux lattice. In this regime, it is shown that this transition is due to quantum fluctuations in the positions of the vortices. From the results of these two experiments, one can piece together the mixed state phase diagram. Upon doing so, it is seen that the Q2D flux solid and vortex liquid states dominate the majority of the phase diagram.

INTRODUCTION

Low dimensional conductors

Anisotropy, or low dimensionality, plays a fundamental role in many areas of contemporary condensed matter physics, both pure and applied. For example, much of the technology that has revolutionized the microelectronics industry in recent years has resulted from the development of low dimensional semiconductor devices. More recently, research into bulk layered materials such as the transition metal oxides [1], organic conductors and superconductors [2], semiconductor superlattices [3], magnetic nanostructure [4], etc., has resulted in the discovery of a range of new physical phenomena, e.g., high temperature superconductivity [5], colossal magnetoresistance [6], and a novel form of the quantum Hall effect [7]. Many of these discoveries challenge basic understanding of condensed matter physics, while, at the same time, may hold the key to further technologies. This thesis will focus on one of the above-mentioned classes of materials; an organic superconductor based on the bis-ethylenedithio-tetrathiafulvalene cation, [abbreviated as BEDT-TTF, or more simply ET (see figure 1)], which has a quasi-two-dimensional (Q2D) character due to its layered crystal structure, and will be discussed in detail below.

BEDT-TTF based conductors and superconductors. In the same way that atoms may be brought together to form conventional solids, large organic molecules may also be used as the basis for building stable crystals, with the added benefit that the crystal properties can be changed by chemically altering the basis molecule [2]. This added

degree of freedom allows chemists to synthesize materials with a wide variety of properties, which depend solely on the underlying chemical structure of the constituent organic molecules. In particular the organic charge transfer salts (CTS), so called due to the partial transfer of electrons between the constituent molecules, have provided a fertile source of novel physical phenomenon, including spin and charge density wave formation, superconductivity, antiferromagnetic behavior, etc [2]. Of the CTS, perhaps the most widely studied family is that based on the BEDT-TTF molecule. The first organic superconductor based on this ET cation was $(\text{ET})_2(\text{ReO}_4)_2$, which was synthesized in 1983, and had the modest T_c of 2.0 K [8]. Shortly after that, many more organic conductors and superconductors followed with the same stoichiometry, $(\text{ET})_2\text{X}$ [2]. Note that although there exist other stable stoichiometries, the 2:1 variety is the most widely studied, and will be the only case considered in this thesis.

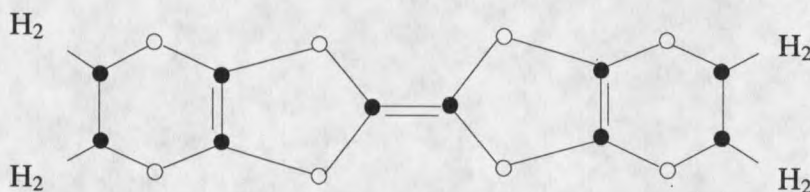
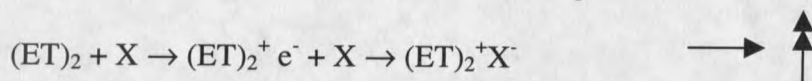


Figure 1. The nominally flat ET molecule. The carbons (●) and sulfurs (○) are strongly σ -bonded within the plane of the molecule, while the π -orbitals on the sulfurs lie perpendicular to the plane of the molecule, and are responsible for the conduction properties of ET based CTS.

For this particular subset of CTS, there is both an ionic and covalent nature to the bonding between the ET cation and the inorganic anion, and between the individual ET cations. Hence, each pair of ET molecules jointly donates a single electron to the anion X, resulting in the following basis for building stable crystal structures [2]:



This is quite similar to the ionic bonding found in traditional inorganic salts such as NaCl. However, as mentioned above, there is also a considerable covalent character to the inter-molecular bonding, which will be shown to give rise to the conduction by these CTS.

Within each ET molecule, the intra-molecular bonds between the atomic species originate from the overlap of hybridized s and p atomic orbitals of the carbon and sulfur atoms within the rings, thereby producing strong σ -bonds [2]. This is quite analogous to the σ -bonding found in the much simpler organic compound, benzene. In this case, the 2s and 2p atomic orbitals hybridize within the plane of the molecule, and overlap to form the σ -bonds between the carbons. This leaves one remaining 2p atomic orbital on each carbon, to form the π -orbitals, which lie normal to the plane of the ring (see figure 2). Whereas the σ -electrons are tightly bound between adjacent carbons in the benzene molecule, the π -electrons are much more loosely bound, and will tend to delocalize around the entire ring [9].

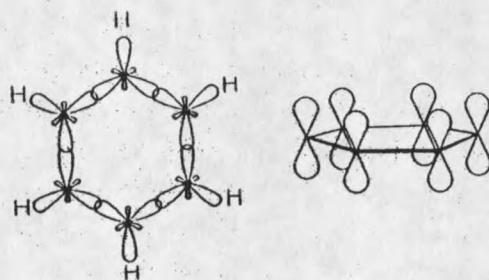


Figure 2. The planar benzene ring. The 2s and 2p atomic orbitals for each carbon hybridize, and then overlap with those on adjacent atoms to form strong σ -bonds (left). The remaining p orbitals lie normal to the plane of the molecule (right) and form the π -orbitals, with loosely bound electrons.

Like benzene, each ET molecule also exhibits π -bonding due to the overlap of the atomic p orbitals of the sulfurs within each ring. However, in the solid state, the π -electrons can delocalize over the entire crystal, rather than solely within a single molecule, so long as there are significant π -orbital overlap. Hence, it is the overlap of the π orbitals within the ET based CTS which are responsible for the bandstructure, i.e., electronic conduction [2].

To understand the band structure of these materials, one must imagine building a crystal one molecule at a time. Thus, if there are N total molecules in the system, then before the solid is assembled, the system will have a series of N-fold degenerate energy levels. However, as the isolated molecules are brought together, that degeneracy is lifted, due to the overlap of π -orbitals between each ET molecule and its neighbors. The energy levels broaden from sharp N-fold degenerate levels into non-degenerate energy bands. The widths of these energy bands will depend explicitly on the amount of inter-molecular π -orbital overlap. This is seen in figure 3 for the simplified case of a hydrogenic atom. On the left side of the figure, the N-fold degenerate atomic energy levels are shown, which broaden into bands as the atoms are brought closer together in the formation of a solid (right side of the figure) [10]. Due to the directional nature of the π orbitals on the ET molecules, i.e., the lobes of the orbitals lie perpendicular to the plane of the ET molecule, the orbital overlap is expected to be highly anisotropic. Consequently, the way in which the molecules pack together to form a crystal structure, will essentially determine the dimensionality of the conductor.

